

# Exclusive diffractive processes in electron-ion collisions

Tobias Toll\* and Thomas Ullrich†  
Brookhaven National Laboratory, Upton, NY  
(Dated: November 27, 2012)

We present a new technique to calculate the cross-section for diffractive vector meson production and DVCS in electron-ion collisions based on the dipole model. The measurement of these processes can provide valuable information on non-linear QCD phenomena, such as gluon saturation, and is the only known way to gain insight into the spatial distribution of gluons in nuclei. We present predictions of differential cross-section distribution  $d\sigma/dQ^2$  and  $d\sigma/dt$  for  $J/\psi$  and  $\phi$  meson production for diffractive processes of heavy nuclei and demonstrate the feasibility of extracting the gluon source distribution of heavy nuclei,  $F(b)$ , from coherent diffraction. We briefly introduce a new event generator based on our method that can be used for studying exclusive diffractive processes at a future electron-ion collider.

## I. INTRODUCTION

The HERA accelerator at DESY, Germany, with collision energies of  $\sqrt{s} = 320$  GeV was the hitherto highest energy lepton-hadron collider. One of the great achievements of HERA was the determination of the partonic structure of the proton [1]. A lepton-hadron collision is mediated by a virtual photon, which interacts with a valence- or sea-quark within the hadron at a resolution  $Q^2$ . When probed at higher energies, gluons fluctuating into gluon- or quark-pairs can be resolved at smaller time scales, such that more partons share the hadron's longitudinal momentum at higher energies. At small momentum fractions  $x \lesssim 10^{-2}$  of the participating partons, measurements at HERA showed that the content of the proton is dominated by gluons, and that the gluon number density at smaller  $x$  seems to rise uncontrollably. When extrapolating current measurements to small  $x$ -values, the gluonic part of the cross-section becomes larger than the total proton cross-section. This violation of the unitarity bound can only be avoided by introducing saturation effects that tame the explosive growth of the gluon density. While many saturation models describing these non-linear effects were developed [2, 3], there exists no *direct* measurement that would allow to verify these models and ultimately prove the existence of gluon saturation. Although more and more tantalizing hints of the onset of gluon saturation coming from proton-ion collisions at RHIC have become available [4–9], alternative explanations can currently not be ruled out [10–12]. The direct study of these non-linear saturation effects would require lepton-hadron collisions at energies far exceeding those at HERA. Electron-ion collisions offer an alternative way to study high gluon-density phenomena at an order of magnitude lower center-of-mass energies. At high enough energies the small  $x$  gluons in the heavy ion have a wave length in the longitudinal direction that encompass the entire width of the nucleus. A probe will thus coherently

interact with the bulk of low- $x$  gluons. For a heavy ion, the thickness is approximately constant away from the edges and is proportional to  $A^{1/3}$ , where  $A$  is its atomic number. This approximate dependence is supported by detailed studies [13, 14]. Therefore, probing a heavy ion with  $A \approx 200$  is similar to probing a proton at 6 times higher energy, making the nucleus an efficient amplifier of the physics of high gluon densities.

There are two proposed future collider projects that aim to directly measure the saturated gluon regime for the first time: the Large Hadron-electron Collider (LHeC) at CERN using the existing LHC machine [15] and the Electron-Ion Collider (EIC) in the USA [17], using either the existing RHIC accelerator complex at BNL (eRHIC), or the existing electron beams at JLab (MEIC).

At HERA, an unexpected discovery was that approximately 10% of the  $ep$  cross-section is from diffractive final states [16] and that this fraction is fairly independent of  $W$  and  $Q^2$ . What characterizes these events experimentally is the presence of a rapidity gap, a region in the angular coverage which exhibits *no* hadronic activity. Diffractive interactions result when the electron probe in DIS interacts with a color neutral vacuum excitation. This vacuum excitation, which in perturbative QCD may be visualized as a colorless combination of two or more gluons, is often called the Pomeron. The hard diffractive cross-section is proportional to the gluon-density *squared*, making it the most sensitive probe of gluon density known. Thus, diffraction and saturation are closely related phenomena.

Measurements of diffraction in an electron-ion collider also have substantial potential to shed light on other unanswered questions in heavy ion collision [17]. Measurements over the last decade in heavy ion collision experiments at RHIC indicate the formation of a strongly coupled plasma of quarks and gluons (sQGP). This sQGP appears to behave like a “near-perfect liquid” with a ratio of the shear viscosity to entropy density ( $\eta/s$ ) approaching  $1/4\pi$  [18–21]. Recent experiments at the LHC with substantially higher energies and thus a hotter and longer lived plasma phase confirm this picture [22]. Despite the significant insight that the sQGP is a strongly correlated nearly perfect liquid, little is understood about how the

\* ttoll@bnl.gov

† thomas.ullrich@bnl.gov

system is created. The largest uncertainty in our understanding of the evolution of a heavy-ion collision comes from our limited knowledge of the initial condition, i.e. momentum and spatial distributions of gluons in the nuclei. Also of importance is how the spatial distribution fluctuates around its mean, since it affects the behavior of collective effects such as flow and their higher moments. For example, different assumptions about the nuclear initial distributions give differences up to factors of two for the obtained  $\eta/s$  value [23, 24]. Measurements of the initial gluon distribution with existing machines are only possible indirectly and with large uncertainties. The study of gluon distributions using diffractive events in electron-ion collisions would allow one to directly measure the initial condition of the colliding ions, providing both its momentum and spatial distributions as well as the underlying fluctuations (“lumpiness”). In fact, exclusive diffractive  $eA$  events are the only way to study the initial spatial distributions and shed light on these fundamental questions.

In a diffractive  $eA$  event, the electron collides with the ion producing one or more extra particles but leaving the nucleus intact. The interaction with the nucleus is either elastic or inelastic, and in the latter case the nucleus subsequently radiates a photon or breaks up into color neutral fragments. When it stays intact, the event is called coherent and when it breaks, the event is called incoherent. The spectrum of the cross-section with respect to the hadronic momentum transfer  $t$  is related to the transverse spatial distribution of the gluons in the ion through a Fourier transform. Also, according to the Good-Walker picture [25], the incoherent cross-section is a direct measure of the lumpiness of the gluons in the ion. In order to access  $t$  in these events, the complete final state has to be measured. This is experimentally only possible in events such as vector-meson production or Deeply Virtual Compton Scattering (DVCS).

At present, the most common approach to calculate diffractive cross-sections at small  $x$  is in the dipole model, where the exchanged virtual photon splits up into a quark anti-quark pair, which forms a color dipole. The dipole subsequently interacts with the target in the target’s rest frame. The dipole model became an important tool for DIS when Golec-Biernat and Wüsthoff (GBW) [26, 27] observed that a simple ansatz for the dipole model integrated over the impact parameter was able to simultaneously describe the total inclusive and diffractive cross-sections. The GBW model also naturally contains saturation in the small  $x$  regime. A shortcoming of the GBW model is that it cannot describe the high  $Q^2$  scaling violation in the inclusive cross-sections measured at HERA, something perfectly described by the collinear DGLAP formalism, which in turn cannot describe the high fraction of diffractive events. This sparked Bartels, Golec-Biernat and Kowalski (BGBK) to include an explicit DGLAP gluon distribution into the dipole formalism [28], taken at a scale directly linked to the dipole size. The BGBK model replicates the GBW model where

it is applicable and also manages to describe the  $Q^2$  dependence of the cross-sections. However, this approach still integrates out the impact parameter dependence of the interaction, without which the  $t$ -dependence of the cross-section is unknown. The impact parameter dependence was introduced in the dipole model by Kowalski and Teaney [30] and then modified to also include exclusive processes by Kowalski, Teaney and Motyka [31]. This dipole model goes by the name bSat (or sometimes IPSat), and is the main focus of this paper.

The bSat model has been studied in detail in the case of electron proton collisions at HERA. There are a few theoretical attempts to expand the bSat model to also describe exclusive  $eA$  collisions (see e.g. [30, 32, 33]). Without exception, these models fail to describe the disappearance of the incoherent cross-section as  $t \rightarrow 0$ . Also, they turn out to be poorly suited for implementation in a Monte Carlo event generator.

In this paper we present the first calculations of not only the coherent but also the incoherent cross-sections in electron-ion collision without making approximations larger than those already inherently present in the bSat model, for all  $t$ . We have implemented the calculation described in this paper in a Monte Carlo event generator (Sartre).

The paper is organized as followed: In section II we will show our derivation of the dipole model in  $eA$ , taking as a starting point the case of  $ep$ . In section III we will present the resulting cross-sections, both as comparisons with HERA data and as predictions for EIC and RHIC.

## II. THE BSAT DIPOLE MODEL

Earlier studies of the dipole model showed that a wide variety of DIS data can be described with only a few assumptions. In particular, it was demonstrated that inclusive DIS can be described together with inclusive charm production and exclusive diffractive vector meson photo- and electro-production. Especially the bSat dipole model is very successful in describing the exclusive production of  $J/\psi$ ,  $\phi$ ,  $\rho$ , and photon (DVCS) production at HERA. Here we only give a short overview of the bSat model in  $ep$  before we discuss its extension to  $eA$  collisions. For a detailed discussion on the bSat model see [31].

### A. A brief description of the bSat dipole model in diffractive $ep$

The amplitude for producing an exclusive vector meson or a real photon diffractively in DIS can be written as:

$$\mathcal{A}_{T,L}^{\gamma^* p \rightarrow V p}(x, Q, \Delta) = i \int dr \int \frac{dz}{4\pi} \int d^2\mathbf{b} (\Psi_V^* \Psi)(r, z) \times 2\pi r J_0([1-z]r\Delta) e^{-i\mathbf{b} \cdot \Delta} \frac{d\sigma_{q\bar{q}}^{(p)}}{d^2\mathbf{b}}(x, r, \mathbf{b}) \quad (1)$$

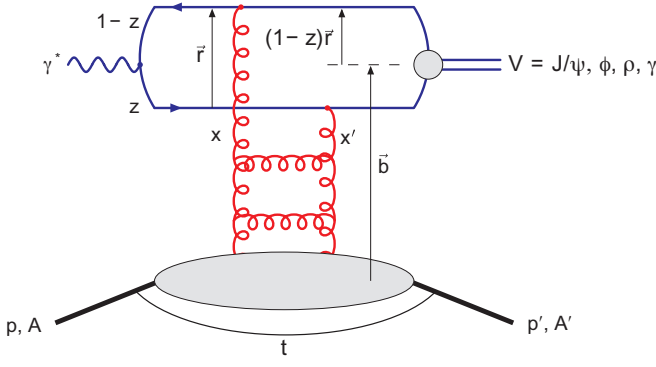


FIG. 1. A schematic picture of the dipole model and its variables. See text for details.

where  $T$  and  $L$  represent the transverse and longitudinal polarizations of the virtual photon,  $r$  is the size of the dipole,  $z$  the energy fraction of the photon taken by the quark,  $\Delta = \sqrt{-t}$  is the transverse part of the four-momentum difference of the outgoing and incoming proton, and  $\mathbf{b}$  is the impact parameter of the dipole relative to the proton (see Fig. 1).  $(\Psi_V^* \Psi)$  denote the wave-function overlap between the virtual photon and the produced vector meson. In this paper we use the "boosted Gaussian" wave-overlap with the parameters given in [31].

The dipole cross-section  $d\sigma_{q\bar{q}}^{(p)}/d^2\mathbf{b}(x, r, \mathbf{b})$  is defined as:

$$\frac{d\sigma_{q\bar{q}}^{(p)}}{d^2\mathbf{b}}(x, r, \mathbf{b}) \equiv 2\mathcal{N}^{(p)}(x, r, \mathbf{b}) = 2[1 - \Re(S)] \quad (2)$$

The first equality is the optical theorem, and we make the approximation of only using the real part of the  $S$ -matrix for the definition of the scattering amplitude  $\mathcal{N}$ , which then becomes a real number between 0 and 1. Here  $(p)$  denotes proton.

In the bSat model the scattering amplitude is:

$$\mathcal{N}^{(p)}(x, r, \mathbf{b}) = 1 - e^{-\frac{\pi^2}{2N_C} r^2 \alpha_S(\mu^2) x g(x, \mu^2) T(\mathbf{b})} \quad (3)$$

where  $\mu^2 = 4/r^2 + \mu_0^2$  and  $\mu_0^2$  is a cut-off scale in the DGLAP evolution of the gluons. The initial gluon density  $xg(x, \mu_0^2) = A_g x^{-\lambda_g} (1-x)^{5.6}$ . The nucleon profile function  $T(\mathbf{b}) = 1/(2\pi B_G) \exp(-b^2/(2B_G))$ . All parameter values are determined through fits to HERA data [31]. For all results in this paper, we use  $B_G = 4 \text{ GeV}^{-2}$ ,  $\mu_0^2 = 1.17 \text{ GeV}^2$ ,  $\lambda_g = 0.02$ , and  $A_g = 2.55$ . Also, the four lightest quark masses are treated as parameters in the model, and are taken to be:  $m_u = m_d = m_s = 0.14 \text{ GeV}$ ,  $m_c = 1.4 \text{ GeV}$ . It should be noted that bSat is a model of multiple two-gluon exchanges at leading log, but some NLL effects are taken into account by the running of the strong coupling.

The total diffractive  $\gamma^*p$  cross-section for this process is:

$$\frac{d\sigma^{\gamma^*p}}{dt} = \frac{1}{16\pi} |\mathcal{A}(x, Q^2, t)|^2 \quad (4)$$

## B. Extending the bSat model from $ep$ to $eA$

The explicit impact parameter dependence of the bSat model makes it especially well suited for the description of processes in  $eA$  collisions. The  $b$  dependence allows one to model the nucleus as a collection of nucleons according to a given nuclear transverse density distribution, e.g. the Woods-Saxon function. To this end we make two observations. Firstly, at small  $x$ , the life-time of the dipole is so large that the dipole traverses the full longitudinal extent of the nucleus. As a consequence the nucleus can effectively be treated as a two-dimensional object in the transverse plane. Also, when the gluon's momentum fraction of the hadron is small, its wavelength in the light-cone direction  $x^-$  becomes so large, that it coherently probes the whole nucleus at  $x \ll A^{-1/3}/(M_N R_p) \sim 10^{-2}$ , where  $M_N$  is the mass of the nucleus and  $R_p$  is the proton radius. Consequently, the information about which nucleon the gluon belongs to is lost, and the exact position of each nucleon within the nucleus is not an observable. In order to calculate the cross-section correctly the average over all possible states of nucleon configurations has to be taken:

$$\frac{d\sigma_{\text{total}}}{dt} = \frac{1}{16\pi} \left\langle |\mathcal{A}(x, Q^2, t, \Omega)|^2 \right\rangle_{\Omega} \quad (5)$$

where  $\Omega$  denotes nucleon configurations.

One defines two different kinds of diffractive events in  $eA$ : coherent and incoherent. In the Good-Walker picture [25] the incoherent cross-section is proportional to the variance of the amplitude with respect to the initial nucleon configurations  $\Omega$  of the nucleus:

$$\frac{d\sigma_{\text{incoherent}}}{dt} = \frac{1}{16\pi} \left( \left\langle |\mathcal{A}(x, Q^2, t, \Omega)|^2 \right\rangle_{\Omega} - |\langle \mathcal{A}(x, Q^2, t, \Omega) \rangle_{\Omega}|^2 \right) \quad (6)$$

where the first term on the R.H.S is the total diffractive cross-section and the second term is the coherent part of the cross-section.

When extending the bSat model from  $ep$  to  $eA$  we will use the independent scattering approximation to construct the scattering amplitude for nuclei:

$$1 - \mathcal{N}^{(A)}(x, \mathbf{r}, \mathbf{b}) = \prod_{i=1}^A \left( 1 - \mathcal{N}^{(p)}(x, \mathbf{r}, |\mathbf{b} - \mathbf{b}_i|) \right) \quad (7)$$

where  $\mathbf{b}_i$  is the position of each nucleon in the nucleus in the transverse plane. We assume that the positions of the nucleons are distributed according to the 3-dimensional Woods-Saxon function projected onto the transverse plane. For details see Appendix A.

Combining equations (2), (3) and (7) the bSat scattering amplitude for  $eA$  becomes:

$$\frac{1}{2} \frac{d\sigma_{q\bar{q}}^{(A)}}{d^2\mathbf{b}}(x, r, \mathbf{b}, \Omega) = 1 - \exp \left( - \frac{\pi^2}{2N_C} r^2 \alpha_S(\mu^2) x g(x, \mu^2) \sum_{i=1}^A T(|\mathbf{b} - \mathbf{b}_i|) \right). \quad (8)$$

Note that the dependence on nucleon configurations  $\Omega$  in the amplitude is entirely contained in this dipole cross-section.

### 1. The incoherent, coherent, and total diffractive cross-sections

In order to obtain the total diffractive cross-section and its coherent part, the second and first moments of the amplitude have to be calculated respectively. For the first moment there is a closed expression for the average of the dipole cross-section [30]:

$$\left\langle \frac{d\sigma_{q\bar{q}}}{d^2\mathbf{b}} \right\rangle_{\Omega} = 2 \left[ 1 - \left( 1 - \frac{T_A(\mathbf{b})}{2} \sigma_{q\bar{q}}^p \right)^A \right] \quad (9)$$

where  $\sigma_{q\bar{q}}^p$  is the  $ep$  dipole cross-section, eq. (3), integrated over the impact parameter, and  $T_A$  is the profile of the Woods-Saxon potential in transverse space.

For the second moment of the amplitude, no analytical expression exists. Similarly as in [29], we derive it by defining an average of an observable  $\mathcal{O}(\Omega)$  over nucleon configurations  $\Omega_i$  by:

$$\langle \mathcal{O} \rangle_{\Omega} = \frac{1}{C_{\max}} \sum_{i=1}^{C_{\max}} \mathcal{O}(\Omega_i). \quad (10)$$

For a large enough number of configurations  $C_{\max}$  the sum on the R.H.S. will converge to the true average. For the total diffractive cross-section one gets:

$$\frac{d\sigma^{\gamma^*A}}{dt}(x, Q^2, t) = \frac{1}{16\pi} \frac{1}{C_{\max}} \sum_{i=1}^{C_{\max}} |A(x, Q^2, t, \Omega_i)|^2. \quad (11)$$

For large  $t$  the variance is several orders of magnitude larger than the average. This means that the convergence of the sum in eq. (10) becomes extremely slow, as demonstrated in Fig. 2(a), where we show the coherent cross-section resulting from averaging over 10, 100, 500, and 800 configurations. As a comparison the "analytical average", i.e. eq. (9) is also shown. As can be seen, not even 800 configurations are enough for convergence at  $-t > 0.15$ .

The convergence of the second moment of the amplitude is shown in Fig. 2(b). We conclude that around 500 configurations are needed to obtain a good description of the cross-section for  $-t < 0.3$ .

### 2. A non-saturated bSat model.

Saturation is introduced in the bSat model through the exponential term in the scattering amplitude (eq. (3)). In order to study the effects of saturation on the production cross-section we construct a non-saturated version of the bSat model by linearizing the dipole cross-section. It should be noted that there is no taming of the rise of

the cross-section for small  $x_P$  or large dipole radii in this case, and studies are only valid where  $\beta = x_P/x_{Bj}$  is large. For exclusive diffraction this is equivalent to keeping  $Q^2$  large. Any other way to impose a limit on the rise of the cross-section, e.g. through a cut-off, inevitably also imposes some form of saturation into the formalism.

In the proton case, the bNonSat dipole cross-section is obtained by keeping the first term in the expansion of the exponent in the bSat dipole cross-section [30]:

$$\frac{d\sigma_{q\bar{q}}^{(p)}}{d^2b} = \frac{\pi^2}{N_C} r^2 \alpha_s(\mu^2) xg(x, \mu^2) T(b). \quad (12)$$

In the case of a nucleus the dipole cross-section becomes:

$$\frac{d\sigma_{q\bar{q}}^{(A)}}{d^2b} = \frac{\pi^2}{N_C} r^2 \alpha_s(\mu^2) xg(x, \mu^2) \sum_{i=1}^A T(|\mathbf{b} - \mathbf{b}_i|) \quad (13)$$

and the coherent part of the bNonSat cross-section can be obtained through the average:

$$\left\langle \frac{d\sigma_{q\bar{q}}^{(A)}}{d^2b} \right\rangle_{\Omega} = \frac{\pi^2}{N_C} r^2 \alpha_s(\mu^2) xg(x, \mu^2) A T_A(b). \quad (14)$$

The parameters we use for the bNonSat model were obtained in [30], by fits to HERA data. They are:  $B_G = 4 \text{ GeV}^{-2}$ ,  $\mu_0^2 = 0.8 \text{ GeV}^2$ ,  $\lambda_g = -0.13$ , and  $A_g = 3.5$ . The bNonSat quark masses are:  $m_u = m_d = m_s = 0.15 \text{ GeV}$ ,  $m_c = 1.4 \text{ GeV}$ .

Figures 3 (a) and (b) shows the wave-overlap  $(\Psi_V^* \Psi)$  between the virtual photon and produced vector mesons as a function of dipole size  $r$ , for transverse and longitudinal polarizations of the photon respectively. The wave-overlap is taken at  $Q^2 = 1 \text{ GeV}^2$  and at  $z = 0.7$ . In Fig. 3 (c) we show the dipole cross-section as a function of dipole size  $r$ . In bSat the rise of the cross-section at large  $r$  is tamed in the model, while in bNonSat it is allowed to rise uncontrollably. Notice that despite the uncontrolled rise of the dipole cross-section, the resulting cross-section stays finite because of the steep fall of the wave-overlap function at large  $r$ . As can be seen in the figure, the lighter (larger) vector mesons  $\rho$  and  $\phi$  are more sensitive to saturation effects than heavier vector meson such as  $J/\psi$ . For  $J/\psi$  the wave-overlap falls off so quickly at large  $r$  that it is an unsuitable probe for accessing the saturated regime, even for large nuclei.

### 3. Phenomenological corrections to the dipole cross-section

In the derivation of the dipole amplitude only the real part of the  $S$ -matrix is taken into account. The imaginary part of the scattering amplitude can be included by multiplying the cross-section by a factor  $(1 + \beta^2)$ , where  $\beta$  is the ratio of the imaginary and real parts of the scattering amplitude. It is calculated using [31]:

$$\beta = \tan\left(\lambda \frac{\pi}{2}\right), \text{ where } \lambda \equiv \frac{\partial \ln(\mathcal{A}_{T,L}^{*\gamma^*p \rightarrow Vp})}{\partial \ln(1/x)}. \quad (15)$$



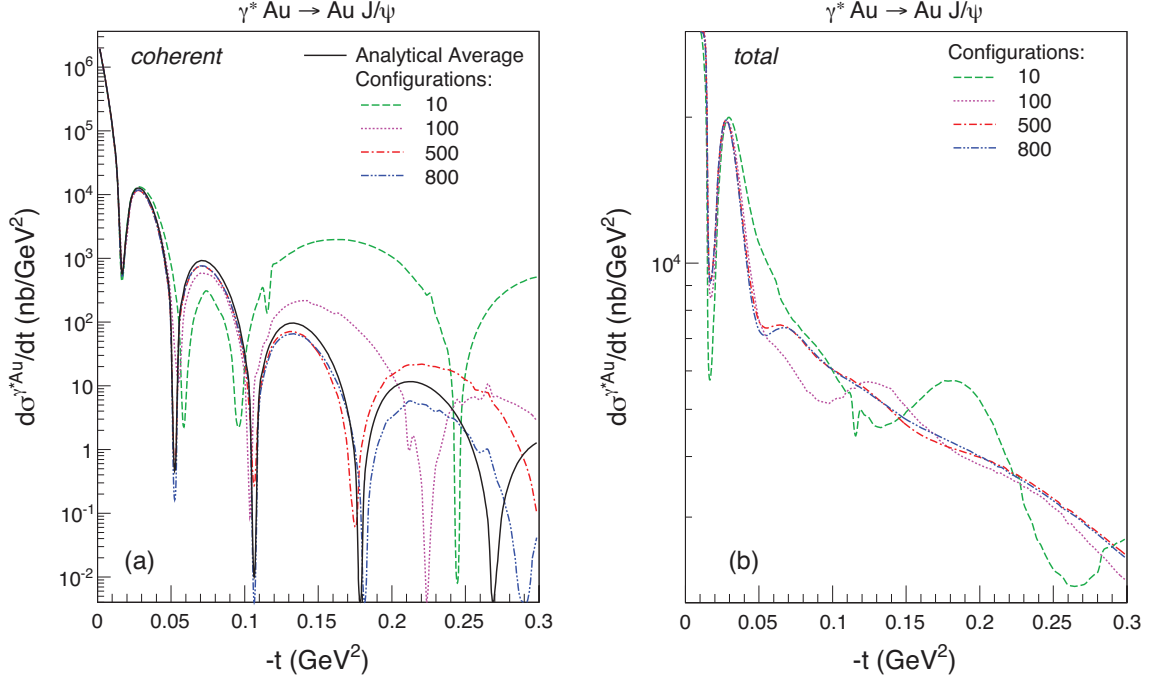


FIG. 2. The resulting coherent (left) and total cross-section (right) for  $\gamma^* A \rightarrow \gamma^* J/\psi A$ , averaged over 10, 100, 500 and 800 configurations. As reference, the coherent analytical average described by eq. (9) is also shown.

In the derivation of the dipole amplitude, the gluons in the two-gluon exchange in the interaction are assumed to carry the same momentum fraction of the proton or nucleus. To take into account that they carry different momentum fractions, a so-called skewedness correction is applied to the cross-section by multiplying it by a factor  $R_g(\lambda)$  defined by [31]:

$$R_g(\lambda) = \frac{2^{2\lambda+3}}{\sqrt{\pi}} \frac{\Gamma(\lambda + 5/2)}{\Gamma(\lambda + 4)} \quad (16)$$

where  $\lambda$  is defined as above. Note that this definition of skewedness-correction for the bSat model is slightly different from the one used in [31], but follows the description in [33].

These corrections are important for describing HERA data, where the models are valid the corrections are typically around 60% of the cross-section, out of which the skewedness correction amounts to around 15%. The corrections grow dramatically in the large  $x$  range outside the validity of the models, where  $x > 10^{-2}$ .

### C. Computing the $eA$ cross-sections

The differential  $ep$  and  $eA$  cross-sections for exclusive diffractive processes cannot be calculated analytically. In order to obtain numerical solutions we have written a computer program to sample and average over nuclear configurations. This program is also the core of a novel event generator, Sartre, which is briefly described in Appendix B.

The total differential cross-section is:

$$\frac{d^3\sigma_{\text{total}}}{dQ^2 dW^2 dt} = \sum_{T,L} \frac{R_g^2(1 + \beta^2)}{16\pi} \frac{dn_{T,L}^\gamma}{dQ^2 dW^2} \langle |\mathcal{A}_{T,L}|^2 \rangle_\Omega \quad (17)$$

where  $dn_{T,L}^\gamma/dQ^2 dW^2$  is the flux of transversely and longitudinally polarized virtual photons, and the average over configurations  $\Omega$  is defined in eq. (10).

The coherent part of the cross-section is:

$$\frac{d^3\sigma_{\text{coherent}}}{dQ^2 dW^2 dt} = \sum_{T,L} \frac{R_g^2(1 + \beta^2)}{16\pi} \frac{dn_{T,L}^\gamma}{dQ^2 dW^2} |\langle \mathcal{A}_{T,L} \rangle_\Omega|^2 \quad (18)$$

while the incoherent part is the difference between the total and coherent cross-sections.

For the the second moment of the amplitude, for each nucleon configuration  $\Omega_i$ , one need to calculate the integral:

$$\begin{aligned} \mathcal{A}_{T,L}(Q^2, \Delta, x_P, \Omega_i) &= \int r dr \frac{dz}{2} d^2\mathbf{b} (\Psi_V^* \Psi)_{T,L}(Q^2, r, z) \\ &\times J_0([1 - z]r\Delta) e^{-i\mathbf{b} \cdot \Delta} \frac{d\sigma_{q\bar{q}}}{d^2\mathbf{b}}(x_P, r, \mathbf{b}, \Omega_i) \quad (19) \end{aligned}$$

where the dipole cross-section is defined in eq. (9) for bSat and in eq. (13) for bNonSat. For  $eA$ , there is no angular symmetry in  $\mathbf{b}$  which makes this integral complex. We average over 500 nucleon configurations, giving 1000 such integrals for each point in phase-space.

For the first moment of the amplitude, the integral to

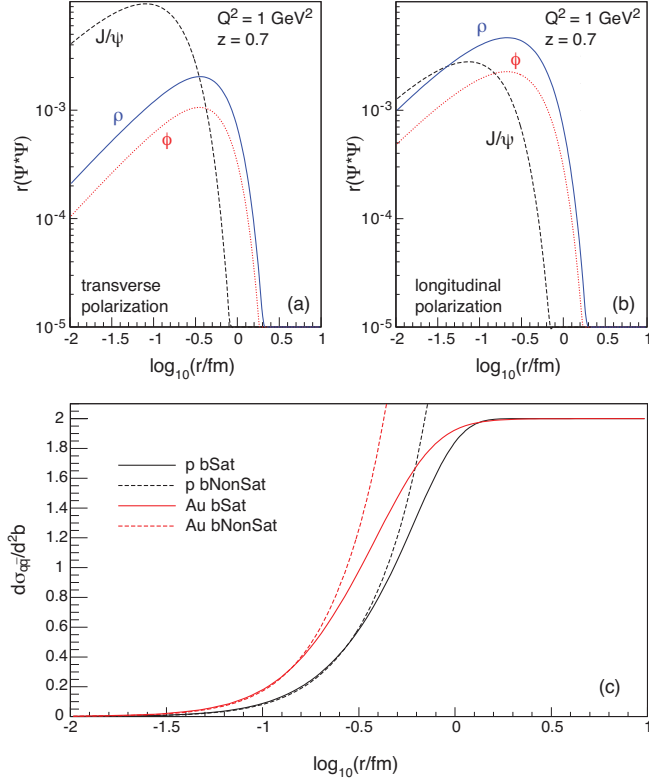


FIG. 3. In (a) and (b) the wave-overlap between the virtual photon and produced vector mesons are shown for transverse and longitudinal polarizations respectively, as functions of dipole radius  $r$ . In the third panel the dipole cross-section is shown as a function of  $r$ , with bSat (solid) and bNonSat (dashed) for protons (black) and gold ions (red/grey).

calculate is:

$$\langle \mathcal{A}_{T,L}(Q^2, \Delta, x_P) \rangle_\Omega = \int \pi r dr dz b db (\Psi_V^* \Psi)_{T,L}(Q^2, r, z) \times J_0([1-z]r\Delta) J_0(b\Delta) \left\langle \frac{d\sigma_{q\bar{q}}}{d^2b} \right\rangle_\Omega(x_P, r, b)(20)$$

where the average in the last term is defined in eq. (9) for bSat and in eq. (14) for bNonSat.

The dipole models described here are only valid for small values of  $x < 10^{-2}$  and not too small values of  $\beta \equiv x/x_P$ . If  $\beta$  becomes too small the  $q\bar{q}$  dipole becomes unphysically large [34]. To rectify this one would need to include higher Fock state dipoles, such as  $q\bar{q}g$ .

### III. RESULTS

In order to verify that our numerical implementation reproduces measured data, we repeated the comparison to the latest HERA data on  $\rho$ ,  $\phi$ ,  $J/\psi$ , and DVCS. We find that both models, bSat and bNonSat, describe HERA data well, within the experimental uncertainties and within the kinematic validity of the models. This is not surprising since the  $ep$  part is a repetition of previous

work ([30, 31]), although our treatment of the skewedness correction differs slightly.

#### A. Predictions for $eA$ collisions

To date, there exist no experimental data on diffractive vector meson production in  $eA$ . However, these measurements are integral parts of the physics programs of future facilities such as the EIC [17] and the LHeC [16]. We show results for  $J/\psi$  and  $\phi$  production. We let the  $J/\psi$  mesons decay into electron pairs, and the  $\phi$  mesons into kaon pairs. The pseudo rapidity and momenta of these decay products are restricted to  $|\eta| < 4$  and  $p > 1$  GeV, respectively. These cuts are made to limit the predictions to an experimentally accessible region of phase-space. We also limit the predictions to  $x < 10^{-2}$  and  $Q^2 > 1$  GeV<sup>2</sup>. We have simulated data corresponding to an integrated luminosity of  $10 \text{ fb}^{-1}$ , with EIC beam energies of 20 GeV for the electron, and 100 GeV/ $u$  for the ion beam. This will amount to a few months of beam operation. The errors shown are statistical only.

In the left hand side panels of Figs. 4 and 5 differential cross-sections with respect to  $Q^2$  for  $J/\psi$  and  $\phi$  production respectively are shown for both bSat and bNonSat models. The cross-sections are scaled by a factor  $A^{4/3}$ . In the dilute limit (large  $Q^2$ ) this scaling is expected to hold for the integral of the coherent peak, which dominates the cross-section, while deviations from it is due to the dense gluon regime. In the right hand side panels the ratio of  $ep$  to  $eA$  cross-sections are shown for both bSat and bNonSat. As can be seen there are significant differences between the two models, something not observed at HERA. Also, the difference is larger for  $\phi$  mesons. The reason for this is that the wave-function overlap between the  $\phi$  meson and virtual photon allows for larger dipoles than that for  $J/\psi$  (see Fig. 3). Therefore,  $\phi$  production can probe further into the dense gluon regime and exhibits larger differences between bSat and bNonSat.

#### Probing the spatial gluon distribution

In Fig. 6 we show the differential cross-section with respect to  $t$ ,  $d\sigma/dt$ , for both  $J/\psi$ - and  $\phi$ -meson production, again for both dipole models. We assume a conservative  $t$ -resolution of 5%, which should be achievable by future EIC detectors. The statistical error bars shown correspond to an integrated luminosity of  $10 \text{ fb}^{-1}$ . As can be seen, the coherent cross-section clearly exhibits the typical diffractive pattern. Also depicted in Fig. 6 is the incoherent cross-section, which is proportional to the lumpiness of the nucleus. Experimentally the sum of the coherent and incoherent parts of the cross-section is measured. Through the detection of emitted neutrons (e.g. by zero-degree calorimeters) from the nuclear breakup in the incoherent case it should be experimentally fea-

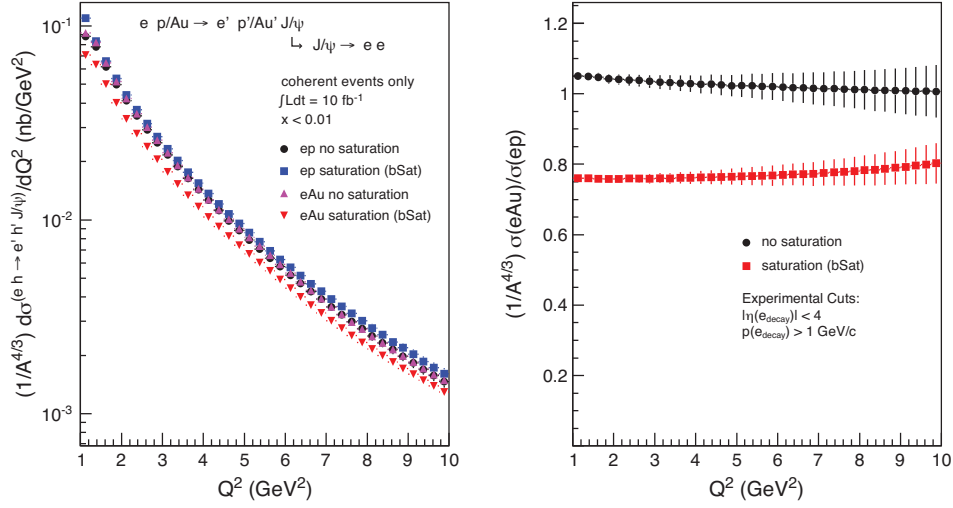


FIG. 4. Left: Cross-sections for  $J/\psi$  production differential in  $Q^2$  for  $ep$  and  $eAu$  collisions for both bSat and bNonSat dipole models. The cross-sections are scaled by  $1/A^{4/3}$ . Right: Ratio of  $eA$  to  $ep$  cross-sections for both models.

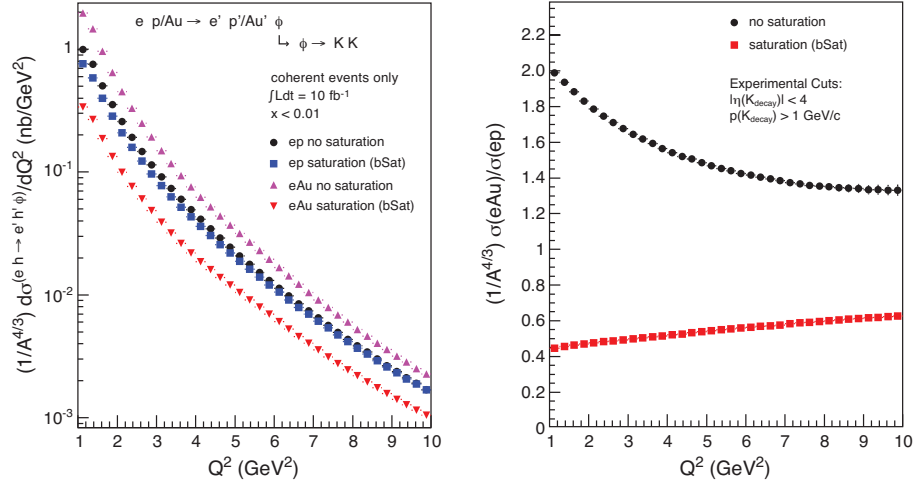


FIG. 5. Left: Cross-sections for  $\phi$  production differential in  $Q^2$  for  $ep$  and  $eAu$  collisions for both bSat and bNonSat dipole models. The cross-sections are scaled by  $1/A^{4/3}$ . Right: Ratio of  $eA$  to  $ep$  cross-sections for both models.

sible to disentangle the two contributions unambiguously.

The coherent distributions in Fig. 6 can be used to obtain information about the gluon distribution in impact-parameter space through a Fourier transform. In eq. (20), the first moment of the diffractive amplitude is a Fourier transform of the dipole cross-section averaged over nucleon configurations, times the wave-function overlap between the vector meson and virtual photon. This represents a transformation from coordinate space to momentum space  $\Delta$ . The coherent cross-section  $d\sigma_{\text{coherent}}/dt$  is proportional to the absolute square of this amplitude. Following [35], we can regain the impact-parameter dependence by performing a Fourier transform on the amplitude. The amplitude can be obtained by taking the square root of the cross-section. In order to maintain the

oscillatory structure of the amplitude we have to switch its sign in every second minimum. We call this modified amplitude  $\sqrt{d\sigma_{\text{coherent}}/dt}|_{\text{mod}}$ . Its Fourier transform is:

$$F(b) = \frac{1}{2\pi} \int_0^\infty d\Delta \Delta J_0(\Delta b) \sqrt{\frac{d\sigma_{\text{coherent}}}{dt}(\Delta)} \Big|_{\text{mod}}, \quad (21)$$

which is a function of impact-parameter only. In our models the impact-parameter dependence comes from the transverse density function  $T_A(b)$ . For bNonSat,  $F(b)$  is directly proportional to the input density function, while for bSat the relation is more complex.

In Fig. 7 we show the resulting Fourier transforms of the coherent curves in Fig. 6, using the range where  $-t < 0.36$  GeV<sup>2</sup>. The obtained distributions have been normalized to unity. For testing the robustness of the

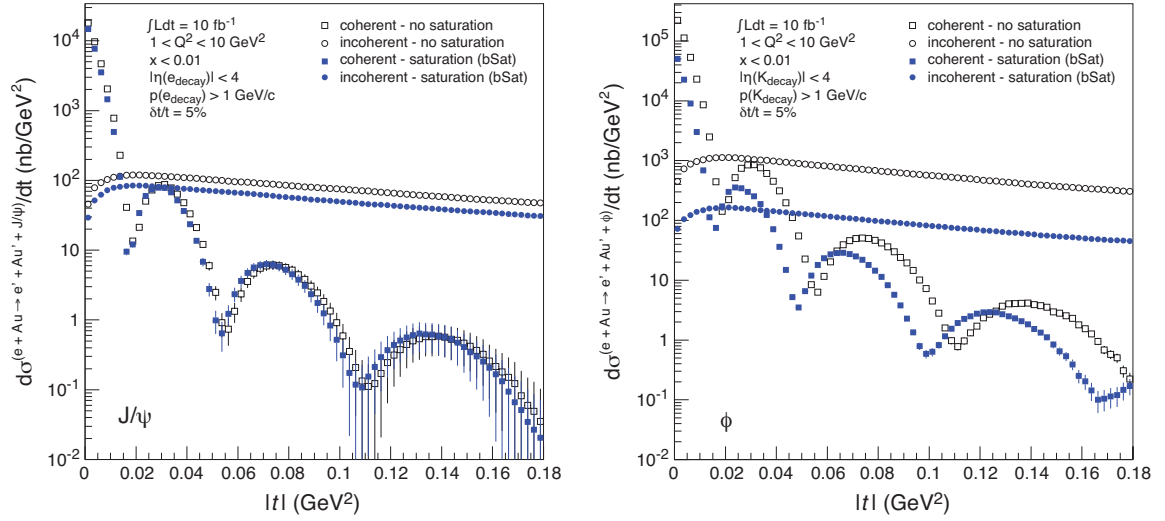


FIG. 6. Differential distributions with respect to  $t$  for exclusive  $J/\psi$  (left) and  $\phi$  (right) for coherent and incoherent events. Both bSat and bNonSat models are shown.

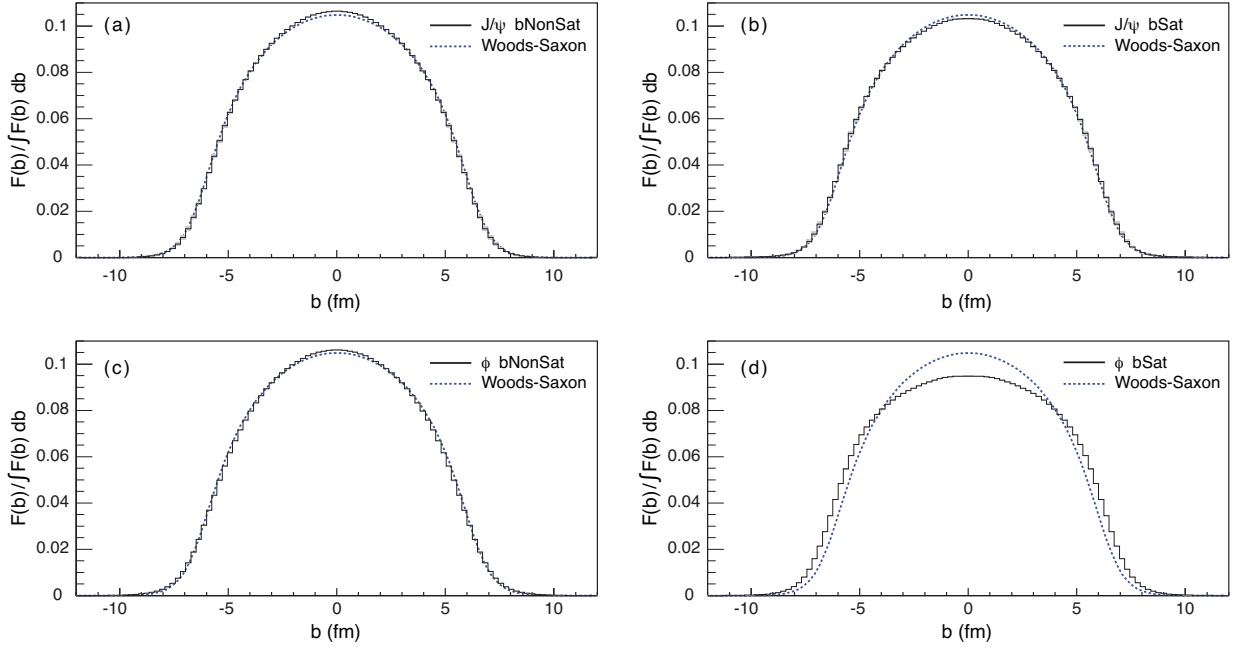


FIG. 7. The Fourier transforms obtained from the distributions in Fig. 6 for  $J/\psi$ -mesons in (a) and (b) and  $\phi$ -mesons in (c) and (d). The results from both bSat and bNonSat are shown with error bands. The input Woods-Saxon distribution is shown as a reference.

method, we used the statistical errors in  $d\sigma/dt$  to generate two enveloping curves,  $d\sigma/dt(t_i) \pm \delta(t_i)$ , where  $\delta$  is the one sigma statistical error in each bin  $t_i$ . The curves are then transformed individually, and the resulting difference defines the uncertainty band on  $F(b)$ . Surprisingly, the uncertainties due to the statistical error are negligible, and are barely visible in Fig. 7.

As a reference we show (dotted line) the original input distribution  $T_A(b)$ , which is the Woods-Saxon function integrated over the longitudinal direction and normal-

ized to unity. The bNonSat curves for  $\phi$ - and  $J/\psi$ -meson production reproduce the shape of the input distribution perfectly as is expected since the bNonSat amplitude is directly proportional to the input distribution. For bSat, the shape of the  $J/\psi$  curve also reproduces the input distribution, while the  $\phi$  curve does not. As explained earlier, this is not surprising, as the size of the  $J/\psi$  meson is much smaller than that for  $\phi$ , which makes the latter more susceptible to differences in the dipole cross-section between bNonSat and bSat, as seen in Fig. 3.



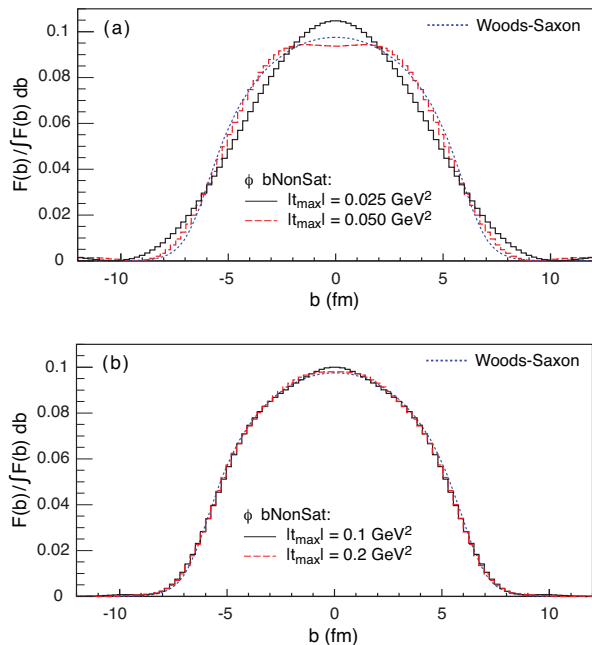


FIG. 8. The Fourier transform of the  $t$ -spectrum of  $\phi$ -meson production in bNonSat, integrated to different upper values of  $|t|$ .

We conclude that the  $J/\psi$  is better suited for probing the transverse structure of the nucleus. However, by measuring  $F(b)$  with both  $J/\psi$ - and  $\phi$  mesons, one can obtain valuable information on how sensitive the measurement is to non-linear effects. Thus, both measurements are important and complementary to each other. The results in Figure 7 provide a strong indication that the EIC and the LHeC will be able to obtain the nuclear spatial gluon distribution from the measured coherent  $t$ -spectrum from exclusive  $J/\psi$  production in  $eA$ , in a model independent fashion.

Strictly, the integral over  $\Delta$  in eq. (21) should be performed up to  $\Delta = \infty$ . In Fig. 8 we demonstrate the effect of finite integration limits, using as an example the  $\phi$  meson curve. We show the transformation for 4 upper values:  $|t|_{\max} = \{0.025, 0.05, 0.1, 0.2\} \text{ GeV}^2$ . The study shows a surprisingly fast convergence towards the input Woods-Saxon distribution.

### B. Ultra Peripheral Collisions

The calculations described in this paper can also be applied to Ultra Peripheral Collisions (UPC) at hadron colliders, such as RHIC and the LHC. At very large impact-parameters between colliding hadrons the long range electromagnetic force becomes dominant over short-range QCD. We substitute the electron's photon flux  $dn^\gamma/dQ^2 dW^2$  in eq. (17) with that from a proton or an ion, as described in e.g. [36].

Process	Cross-section (nb)
$p + p$	0.716
$p + \text{Au}$	$0.666 \cdot 10^3$
$\text{Au} + \text{Au}$	$1.22 \cdot 10^6$

TABLE I. Cross-sections of  $J/\psi$  in UPC events at RHIC. All cross-sections are for  $\sqrt{s} = 200 \text{ GeV}/u$ ,  $10^{-6} \leq Q^2 \leq 1 \text{ GeV}^2$ ,  $4 \leq W \leq 142 \text{ GeV}$ ,  $0 \leq -t \leq 0.3 \text{ GeV}^2$ .

In Table I we list the predicted cross-sections for  $J/\psi$  mesons produced exclusively at RHIC energy in  $p + p$ ,  $p + \text{Au}$ , and  $\text{Au} + \text{Au}$  collisions. Each cross-section is a sum of the two possible photon directions in the events, such that symmetric beam particles are multiplied by a factor 2, and the  $p + \text{Au}$  cross-section is the sum of the photon coming from the proton and from the gold-ion respectively. Especially for light mesons such as  $\phi$ , these studies might provide new constraints for non-linear phenomena, such as saturation. Measurements at existing hadron colliders are still limited in statistics at the time of writing but more detailed measurements will become available soon. The PHENIX experiment at RHIC measured the central UPC diffractive  $J/\psi$ -production cross-section at  $\sqrt{s} = 200 \text{ GeV}$ , for  $|\eta(J/\psi)| < 0.35$  corresponding to  $21 < W < 30 \text{ GeV}$ , when the  $J/\psi$  decays into an electron pair [37]. The resulting cross-section is measured to be  $d\sigma/dy = 76 \pm 33(\text{stat.}) \pm 11(\text{syst.}) \mu\text{b}$ . Our result is  $d\sigma/dy = 54.9 \mu\text{b}$ , which is well within the experimental uncertainty.

## IV. CONCLUSIONS

We have presented a new method for calculating exclusive diffractive vector meson and DVCS production in high energy  $eA$  collisions, based on the dipole model. This method is the first to describe incoherent  $eA$  collisions without making approximations larger than those already inherently present in the dipole model, for all values of  $t$ . In some parts of phase-space, the cross-section is dominated by its incoherent part, which is thus essential for making realistic predictions for future  $eA$  experiments. High energy  $eA$  collisions are expected to be sensitive to non-linear saturation effects. We have therefore implemented our method in two dipole models: the bSat model and its linearization the bNonSat model.

In Figs. 4 and 5 we show that in an  $eA$  collider, the two models are clearly distinguishable, which is not the case in previous  $ep$  experiments. We also show that  $\phi$ -meson production is considerably more sensitive to non-linear effects than  $J/\psi$ -meson production. This is due to the larger size of the wave-function overlap for the  $\phi$ -meson. In Figs. 6 and 7, we show that one can probe the transverse spatial gluon distribution of a nucleus by performing a Fourier transform of the measured coherent  $t$ -spectrum. This method is very robust with respect to statistical uncertainties and only requires a range of

$t \lesssim 0.2 \text{ GeV}^2$  for gold. Due to its smaller wave function, the  $J/\psi$ -meson is considerably more suitable for probing the spatial gluon distribution than the lighter  $\phi$ -meson. In Fig. 6 we also show the incoherent  $t$ -spectrum, which is directly proportional to the lumpiness of the initial nucleus. Our method can also be used to calculate UPC events in present hadron-hadron colliders. We describe central  $J/\psi$  data from the PHENIX experiment well within the experimental uncertainties.

## ACKNOWLEDGMENTS

The authors would like to thank Henri Kowalski, Tuomas Lappi, and Raju Venugopalan for their input and help, and the Open Science Grid consortium for providing resources and support. This work was supported by the U.S. Department of Energy under Grant No. DE-AC02-98CH10886.

### Appendix A: Generating a nucleon configuration according to the Woods-Saxon potential

We generate the nucleus according to the Woods-Saxon distribution, which is assumed to describe the number density of nucleons per volume element, i.e.:

$$\frac{d^3N}{d^3\mathbf{r}} = \rho(r) = \frac{\rho_0}{1 + e^{\frac{r-R_0}{d}}} \quad (\text{A1})$$

where  $\rho_0$  is the central density,  $R_0$  is the radius of the nucleus and  $d$  is the skin thickness which describes how fast the potential falls off close to the edge of the nucleus. The parameters  $\rho_0$ ,  $R_0$  and  $d$  have been measured for most nuclei in low-energy experiments [38].

Our method for generating a nucleus is as follows:

1. We first generate the radial distribution of all nucleons in a given nucleus specimen according to:

$$\frac{dN}{dr} = 4\pi r^2 \rho(r), \quad (\text{A2})$$

and sort them in  $r$ .

2. We then generate the angular distributions uniformly in azimuthal angle,  $\phi$ , and polar angle,  $\cos\theta$ , one at a time beginning with the innermost nucleon.
3. If the newly generated nucleon position is within a core distance of 0.8 fm from any other nucleon

we regenerate  $\phi$  and  $\cos\theta$ , keeping the original  $r$ . If this fails repeatedly, we drop the nucleus and restart from 1.

4. Finally, when all nucleons have been placed, the origin of the nucleus is shifted to its center of mass.

### Appendix B: Generating events with Sartre

Sartre is a novel Monte Carlo event generator, implementing the models described in this paper. It generates exclusive events in diffractive vector meson and DVCS production for  $ep$  and  $eA$  collisions.

The master equation of Sartre is eq. (17). In the event generator, this cross-section is simply used as a probability density function from which a phase-space point in  $Q^2$ ,  $W^2$ , and  $t$  is drawn. Given the beam energies and these three kinematic variables, the final state of the event is fully defined except for the azimuthal angle of the vector meson, which is uniformly distributed.

To determine the total cross-section in  $eA$ , the complex four-dimensional integral described in eq. (19) has to be calculated for each phase-space point 1000 times, which is prohibitive for efficient event generation. Therefore, we tabulate the first and second moments of the amplitudes, for both longitudinally and transversely polarized photons separately. The resulting look-up tables are three dimensional in  $Q^2$ ,  $W^2$  and  $t$ . There is a set of four look-up tables ( $\langle |\mathcal{A}_T|^2 \rangle$ ,  $|\langle \mathcal{A}_T \rangle|$ ,  $\langle |\mathcal{A}_L|^2 \rangle$ ,  $|\langle \mathcal{A}_L \rangle|$ ) for each species of produced vector meson or DVCS, and for each species of nucleus.

When an event has been generated it is decided probabilistically whether the event was coherent or incoherent by comparing the coherent cross-section in eq. (18) with the total one. In the incoherent case we let the nucleus break up by assuming that the diffractive mass  $M_Y$  is distributed according to:

$$\frac{dN}{dM_Y^2} \propto \frac{1}{M_Y^2}. \quad (\text{B1})$$

Note that  $M_Y$  cannot be uniquely determined from kinematics alone. The corresponding excitation energy of the nucleus is:

$$E^* = (M_Y - m_n) \cdot A \quad (\text{B2})$$

We then use this excitation energy as input for Gemini++ [39], a statistical model code which describes the nuclear de-excitation, providing the break-up products from neutrons up to the heaviest fragments.

- 
- [1] F. D. Aaron *et al.* [H1 and ZEUS Collaboration], JHEP **1001**, 109 (2010) [arXiv:0911.0884 [hep-ex]].  
 [2] E. Iancu and R. Venugopalan, In \*Hwa, R.C. (ed.) et al.:

- Quark gluon plasma\* 249-3363 [hep-ph/0303204].  
 [3] H. Weigert, Prog. Part. Nucl. Phys. **55**, 461 (2005) [hep-ph/0501087].

- [4] I. Arsene *et al.* [BRAHMS Collaboration], Phys. Rev. Lett. **93**, 242303 (2004) [nucl-ex/0403005].
- [5] J. Adams *et al.* [STAR Collaboration], Phys. Rev. Lett. **97**, 152302 (2006) [nucl-ex/0602011].
- [6] E. Braidot [STAR Collaboration], Nucl. Phys. A **854**, 168 (2011) [arXiv:1008.3989 [nucl-ex]].
- [7] A. Adare *et al.* [PHENIX Collaboration], Phys. Rev. Lett. **107**, 172301 (2011) [arXiv:1105.5112 [nucl-ex]].
- [8] J. L. Albacete and C. Marquet, Phys. Rev. Lett. **105**, 162301 (2010) [arXiv:1005.4065 [hep-ph]].
- [9] T. Lappi and H. Mantysaari, arXiv:1209.2853 [hep-ph].
- [10] M. Strikman and W. Vogelsang, Phys. Rev. D **83**, 034029 (2011) [arXiv:1009.6123 [hep-ph]].
- [11] Z. -B. Kang, I. Vitev and H. Xing, Phys. Rev. D **85**, 054024 (2012) [arXiv:1112.6021 [hep-ph]].
- [12] Z. -B. Kang, I. Vitev and H. Xing, arXiv:1209.6030 [hep-ph].
- [13] H. Kowalski, T. Lappi, and R. Venugopalan, Phys. Rev. Lett. **100**, 022303 (2008).
- [14] H. Kowalski and D. Teaney, Phys. Rev. **D68**, 114005 (2003), arXiv:hep-ph/0304189.
- [15] J. L. Abelleira Fernandez *et al.* [LHeC Study Group Collaboration], J. Phys. G **39**, 075001 (2012) [arXiv:1206.2913 [physics.acc-ph]].
- [16] H. Abramowicz and A. Caldwell, Rev. Mod. Phys. **71**, 1275 (1999) [hep-ex/9903037].
- [17] EIC White Paper, in preparation.
- [18] K. Adcox *et al.* [PHENIX Collaboration], Nucl. Phys. A **757**, 184 (2005) [nucl-ex/0410003].
- [19] J. Adams *et al.* [STAR Collaboration], Nucl. Phys. A **757**, 102 (2005) [nucl-ex/0501009].
- [20] B. B. Back, M. D. Baker, M. Ballintijn, D. S. Barton, B. Becker, R. R. Betts, A. A. Bickley and R. Bindel *et al.*, Nucl. Phys. A **757**, 28 (2005) [nucl-ex/0410022].
- [21] I. Arsene *et al.* [BRAHMS Collaboration], Nucl. Phys. A **757**, 1 (2005) [nucl-ex/0410020].
- [22] I. Tserruya, AIP Conf. Proc. **1422**, 166 (2012) [arXiv:1110.4047 [nucl-ex]].
- [23] Z. Qiu and U. W. Heinz, Phys. Rev. C **84**, 024911 (2011) [arXiv:1104.0650 [nucl-th]].
- [24] S. Esumi [PHENIX Collaboration], J. Phys. G **38**, 124010 (2011) [arXiv:1110.3223 [nucl-ex]].
- [25] M. L. Good, W. D. Walker, Phys. Rev. **120**, 1857-1860 (1960).
- [26] K. J. Golec-Biernat and M. Wusthoff, Phys. Rev. D **59**, 014017 (1998) [hep-ph/9807513].
- [27] K. J. Golec-Biernat and M. Wusthoff, Phys. Rev. D **60**, 114023 (1999) [hep-ph/9903358].
- [28] J. Bartels, K. J. Golec-Biernat and H. Kowalski, Phys. Rev. D **66**, 014001 (2002) [hep-ph/0203258].
- [29] B. Z. Kopeliovich, J. Nemchik, A. Schafer and A. V. Tarasov, Phys. Rev. C **65**, 035201 (2002) [hep-ph/0107227].
- [30] H. Kowalski and D. Teaney, Phys. Rev. D **68**, 114005 (2003) [hep-ph/0304189].
- [31] H. Kowalski, L. Motyka, G. Watt, Phys. Rev. **D74**, 074016 (2006). [hep-ph/0606272].
- [32] A. Caldwell and H. Kowalski, Phys. Rev. C **81**, 025203 (2010).
- [33] T. Lappi and H. Mantysaari, Phys. Rev. C **83**, 065202 (2011) [arXiv:1011.1988 [hep-ph]].
- [34] H. Kowalski, T. Lappi, C. Marquet and R. Venugopalan, Phys. Rev. C **78**, 045201 (2008) [arXiv:0805.4071 [hep-ph]].
- [35] S. Munier, A. M. Stasto and A. H. Mueller, Nucl. Phys. B **603**, 427 (2001) [hep-ph/0102291].
- [36] S. R. Klein and J. Nystrand, Phys. Rev. Lett. **84**, 2330 (2000) [hep-ph/9909237].
- [37] M. Csanad [PHENIX Collaboration], arXiv:0907.4856 [nucl-ex].
- [38] C. W. De Jager, H. De Vries and C. De Vries, Atom. Data Nucl. Data Tabl. **14**, 479 (1974).
- [39] R. J. Charity, "Advanced Workshop on Model Codes for Spallation Reactions" (Trieste, Italy: IAEA) p 139 report INDC(NDC)-0530